



On asymmetric compound open channel flows with two distinct width floodplains: revisiting interfacial mixing layer and flow structures

Prateek Singh¹ · Xiaonan Tang¹ · Hamdoon Ijaz²

Received: 12 December 2022 / Accepted: 15 May 2023 / Published online: 4 June 2023
© The Author(s), under exclusive licence to Springer Nature B.V. 2023

Abstract

In high-flow events, inland surface flow cross sections are defined as compound staged channels with irregular and asymmetric nature of floodplains. Understanding the transverse exchange processes of mass and momentum in compound channel sections with different floodplain widths is essential as these effects are linked directly to the riverbank stability, sedimentation and nutrient transport. Three configurations were tested to study time-averaged lateral flow, advection transport of momentum, and their interaction with the shear layer turbulence over different-sized floodplains in compound open channels. Three factors, viz. depth-averaged flow, shear layer turbulence, and dispersive term of transverse velocity, are assessed to investigate this interaction. The 3D flow structures over the different-sized floodplains in the compound channels were studied using the power density spectral and the quadrant analysis of Reynolds shear stresses to reveal the coherent structure effect over the transverse exchange of momentum in these new test cases. The results showed that the transverse exchange and eddy viscosity for the asymmetric compound channels with two floodplains have a higher magnitude than the symmetric compound channel due to higher momentum redistribution over distinct floodplain widths. The shear layer tends to shift towards a stronger transverse current side for the new asymmetric compound channels with different floodplain widths. Irrespective of roughness, more significant mixing layers are commonly viable on the smaller floodplain. The floodplains' size and roughness strongly influence the main channel shear layer width dynamics.

Keywords Compound channel flow · Asymmetrical channels · Experimental studies · Momentum exchange · Power spectral quadrant · Coherent structures · Reynolds shear stress

✉ Xiaonan Tang
Xiao.Tang@xjtlu.edu.cn

Prateek Singh
p.singh@alumni.xjtlu.edu.cn

Hamdoon Ijaz
hamdoonijaz1@outlook.com

¹ Department of Civil Engineering, Xi'an Jiaotong-Liverpool University, Suzhou, China

² Department of Aeronautics and Aviation Engineering, The Hong Kong Polytechnic University, Hung Hom, Hong Kong

List of symbols

B	Top width (m) of channel
b	Main channel width (m)
b_f	Floodplain width (m)
Dr	Depth ratio ($\frac{H-h}{H}$)
g	Gravitational acceleration (m/s^2)
h	Height of bankfull (m)
H	Total depth of flow (m)
L	Length of the channel (m)
n_c	Manning's coefficient n for the main channel
n_f	Manning's coefficient n for the floodplain
S_o	Bed slope
S_w	Water surface elevation slope
Q1, Q2, Q3, Q4	Velocity-intermittency quadrants
U_{ave}	Overall average velocity (m/s)
$U_{x,d}$	Depth-averaged streamwise velocity (m/s)
$U_{x,c}$	Averaged streamwise main channel velocity (m/s)
$U_{x,int}$	Depth-averaged streamwise interfacial velocity (m/s)
$U_{x,p}$	Averaged streamwise floodplain velocity (m/s)
U_x, U_y, U_z	Time-averaged velocities (m/s)
$U_{y,d}$	Depth-averaged transverse velocity (m/s)
$\frac{dU_x}{dy}$	The gradient of velocity ($1/s$)
u'_x, u'_y, u'_z	Fluctuation velocities (m/s)
u_x, u_y, u_z	Instantaneous velocity (m/s)
u'^2_y, u'^2_x	Turbulent intensities (m^2/s^2)
$x-, y-, \text{ and } z-$	Streamwise, transverse, and vertical axes (m)
ε_a	Eddy viscosity
δ_c, δ_f	The transverse shear layer of the main channel and floodplains (m)
σ_z, σ_x	Standard deviations of the vertical and streamwise velocities
τ_a	Apparent shear stress (N/m^2)
δ	Transverse shear layer (m)
$\overline{\rho u'_x u'_y}, \overline{\rho u'_x u'_z}$	Reynolds shear stress (N/m^2)
ρ	Density (kg/m^3)

Abbreviations and Subscripts

ADV	Acoustic Doppler Velocimeter
PSD	Power spectral density
RSS	Reynolds Shear Stress
SNR	Signal-to-Noise ratio
R	Rectangular cross-section
RR	Rough rectangular cross-section
c	Subscript for the main channel
f	Subscript for floodplain(s)

1 Introduction

The compound open channels are categorised as symmetric and asymmetric based on geometry and homogenous and heterogeneous based on roughness. An inland river in a two-stage geometry during high flow season has a main channel, and adjacent floodplain(s) (Fig. 1), as commonly exist in nature. An asymmetric cross-section in compound open channel flow usually defines the geometrical representation of the floodplains adjacent to the main channel. Asymmetrical floodplains can either be a single floodplain or have a distinct geometrical size with identical or varying roughness around the main channel. The interaction of these different subsections, which include a deeper main channel and shallower floodplains, have a shearing effect on the bank's interface.

Due to the difference in velocity between the deeper flow in the main channel and the shallower flow in the adjacent floodplain(s), a lateral mixing layer is created, resulting in three-dimensional features owing to the complex geometry and the vertical confinement of the flow [1–4]. The present study aims to investigate the streamwise steady uniform flow in such asymmetric channels, which have differential floodplain widths, as depicted in Fig. 1. This study will help to understand the shear mixing layer of parallel flows in the new compound channel configurations with smooth and rough floodplains of different widths. The effect of wall proximity is also discussed for the mixing layer between the main channel and floodplains for these particular asymmetric and symmetric channels. The mixing layer plays a significant role in the redistribution of momentum within the cross-section of the river, accelerating the floodplain flow [5, 6]. The experimental investigation of momentum

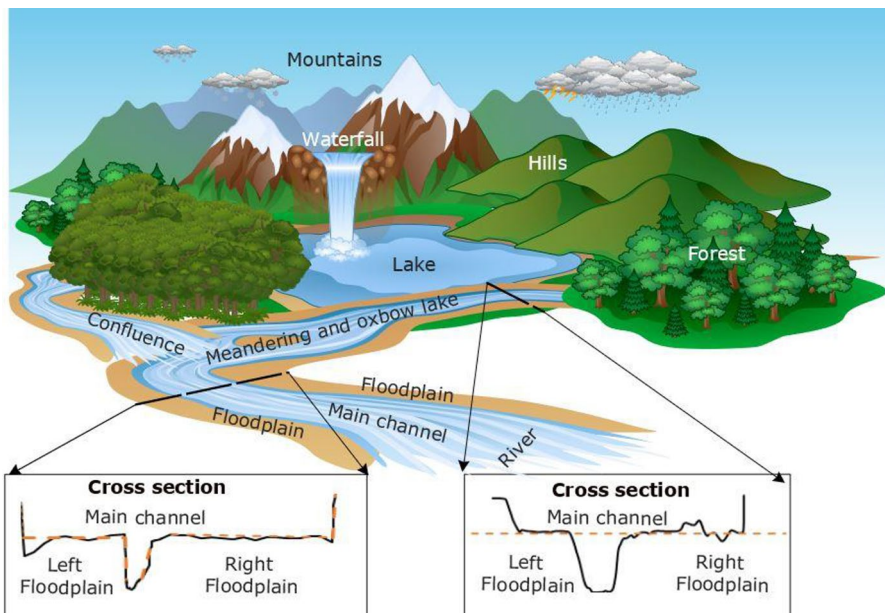


Fig. 1 Conceptual depiction of the real-time riverine inland flow having two distinct cross sections with asymmetric characteristics. The cross sections have different widths of the left and right floodplain(s). The dotted line depicts the approximation of the irregular cross-section of the natural river into rectangular cross-sections at high (right) and regular (left) flow events

distribution led to apparent shear stress over zero shear line estimation for specific compound channels will help in the development of one-dimensional lucid models for stage, zonal and overall discharge estimation [7–13].

Previously, Knight and Demetriou [14], Knight and Hamed [15], and Tominaga and Nezu [16] pointed out that the geometrical driving variables of a straight compound channel flow include: the depth ratio (D_r : the ratio of the depths between the floodplain and the main channel); the total width-to-depth ratio of the main channel; the ratio of main channel width to total depth; the ratio of roughness over floodplain(s) and main channel; and for trapezoidal section, also the bank slopes of the main channel and floodplain(s). The decrease in flow depth over the floodplain or the increase in the difference of the roughness over the floodplain and main channel results in the increasing velocity difference across the mixing layer, which catapults the turbulence production [17]. The effect of the depth ratio and the total width-to-depth ratio in the main channel and the bank slope play a significant role in the process of momentum distribution and also dictate the formation of the secondary currents over the compound cross-section [16, 18, 19].

Atabay [20] demonstrated that the apparent shear force on the vertical and horizontal interface of the symmetric and asymmetric with one-floodplain compound open channels has distinct order of magnitude for the comparative geometrical dimensions. For the same aspect ratio (ratio of channel width to the flow depth) and the depth ratio, symmetric (identical two floodplains) and asymmetric (only one floodplain on the side of the main channel) compound sections lead to different flow fields [21]. In a symmetrical cross-section, mixing layers at both sides of the main channel can meet at the main channel centerline [4]. Meanwhile, in the asymmetrical cross-section, the mixing layer can reach the lateral boundary layer of the vertical wall. In the following new configuration of the asymmetric compound channel with differential floodplain width, a turbulent mixing layer formed at the two consecutive flow sections—left and right floodplains—will help to understand the flow dynamics closer to the natural inland flow conditions. From a practical point of view, bulk or averaged velocity difference between the main channel and floodplain(s) will better define the mixing layer over the different ranges of flow depth [22–24].

Previously, compound channel flows were investigated in a laboratory backdrop through experimentation, which covered different types of asymmetric compound channels: smooth bed [20, 25–28], rough bed [29–32], and emergent macro roughness [33–37]. Figure 2 depicts the broad spectrum of the experimental studies available for the asymmetric compound channels with a single floodplain. However, in the previous studies, the effect of the floodplains' width on the shear layer width distribution has never been targeted experimentally to distinguish the flow behaviour over symmetric and differential floodplains' asymmetric compound channels. Therefore, the present paper investigates the new configuration of the asymmetric compound open channel for smooth and rough floodplains at five-depth ratios. The rough floodplain was fabricated using synthetic grass with very high density and small blade length, depicting the grassland biome's natural condition or the artificial turf over the riverbank [38–40]. The flow conditions are such that two flow regimes in this study were defined as shallow flow ($D_r < 0.3$) and intermediate flow ($0.3 < D_r < 0.5$) as per Nezu et al. [41] and Stocchino and Brocchini [42]. The shallow flow characteristic is established through the interface's monotonic and strong gradient of velocity flow. More specifically, experimental studies of the asymmetric channels with two floodplains were presented to understand the effects of the depth ratio on differential floodplain width.

Furthermore, we investigated the interaction of the floodplain(s) and main channel by determining time-averaged transverse flow caused by the shear layer turbulence generated by the complex asymmetric cross-section. The three contributing factors of transverse

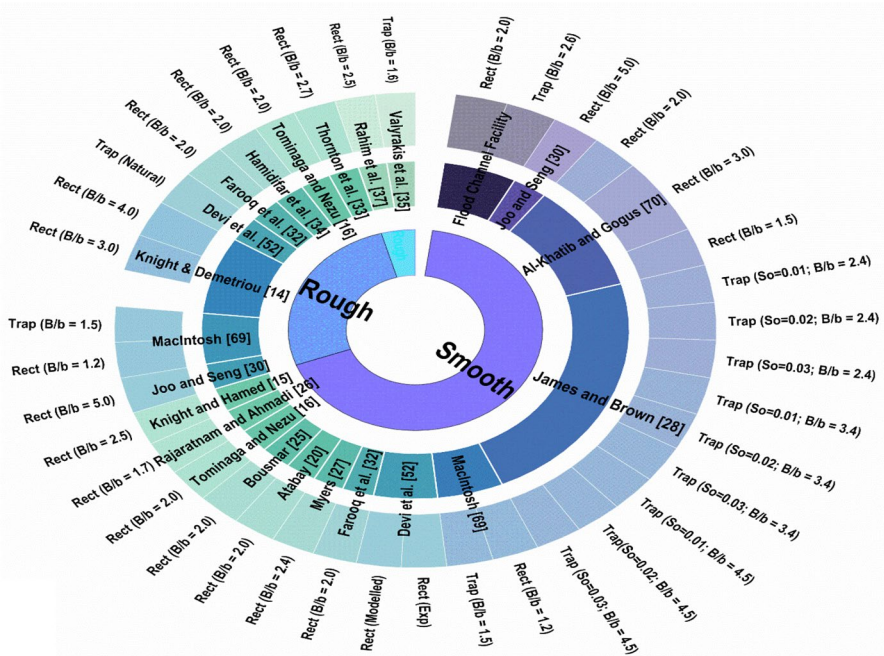


Fig. 2 The categorical representation of datasets on the asymmetric compound open channel flows with a single floodplain

momentum flux are estimated here: depth-averaged lateral Reynolds shear stress, a dispersive term of transverse velocity over different depths, and velocity components. Eddy viscosity approach over the vertical interface between the main channel and floodplain(s) was given since it is critical in one-, two-, pseudo-two-, and three-dimensional numerical modelling [43–46]. The experiments conducted for the different configurations were compared, and the effect of the depth ratio on the mass and momentum exchange in uniform flow was investigated and presented for the present novel test cases.

To understand the flow characteristics of such asymmetric compound channels, in subsequent sections, the present paper is arranged as follows: a short critical review of asymmetric compound channels, followed by an experimental setting, then a comprehensive analysis and discussion of results on transverse distributions of time-averaged velocity quantities, Reynolds stress, turbulence intensities, flow interaction between the main channel and floodplains, eddy viscosity and momentum flux at the interface, and coherent structures. Finally, a conclusion is drawn.

2 A critical review of asymmetric compound open channel flows

Figure 2 outlines the earlier studies of smooth and rough asymmetric compound open channels. From the comprehensive data set here, one can identify that the research gap remains in the missing experimental analysis for the channels with a higher aspect ratio (b/h) of the main channel width to the bankfull height deliberated in Table 1. The whole

Table 1 Dataset of geometrical parameters combination explored in previous studies for asymmetric compound open channel flows

Code	Reference	Type	Bed Condition	L/B	b/h	B/b	b_f/b	Slope* 10^{-3}
AS1	FCF Series 06	Asymmetric	Smooth	6	10	4.2	1.5	1.027
AS2.1	Devi et al. [52]	Asymmetric	Smooth	8.9–12.6	3	3.6–5.1	2.3–3.7	1.238
AS2.2		Asymmetric Natural River	River Trent	NA	7.3	5.14	3.43	1
AS2.3		Asymmetric Modeled	CES Channels	NA	3 & 10	7–12	4.9–10.9	1.027 & 1.238
AS3	Farooq et al. [32]	Asymmetric	Both	41.67	0.34	2	1	0.1–0.2
AS4.1–4.9	Al-Khatib et al. [31]	Asymmetric	Smooth	25	1.25–3.75	1.5–3	0.5–2	2.5
AS5.1–5.9	Al-Khatib et al. [31]	Asymmetric	Smooth	25	1.25–3.75	1.5–3	0.5–2	2.5
AS6.1–6.3	Joo and Seng [30]	Asymmetric	Rough	40	1	2.8–5	1.8–4	13
AS7	Hamidifar et al. [34]	Asymmetric	Emergent Rough	22.23	3.2	2	1	0.88
AS8	Myers [27]	Asymmetric	Smooth	15.25	2.5	2.4	1.4	0.264
AS9	Atabay [20]	Asymmetric	Smooth	15	7.96	2.02	1.02	2.024
AS10	Bousmar [25]	Asymmetric	Smooth	12.5	8	2	1	0.99
AS11.1–11.3	James and Brown [28]	Asymmetric	Smooth	2.8–5.34	3.5	2.3–4.5	1.07–3.21	1–3
AS12.1–12.4	Tominaga and Nezu [16]	Asymmetric	Smooth S1	31.25	10	2	1	2
			Smooth S2		5			
			Smooth S3		3.3			
			Rough R1		5			
AS13.1–13.4	Knight et al. [29]	Asymmetric	S10 Rough	24.5	2	4.01	3.01	2.024
			S11 Rough	32.9		3	2	
			S12 Rough	49.3		2	1	
			S15 Smooth	19.7		5.01	4.01	
AS14	Thornton et al. [33]	Asymmetric with vegetation	Vegetation with low density and without vegetation	12.3	3.06	2.65	1.65	2

Table 1 (continued)

Code	Reference	Type	Bed Condition	L/B	b/h	B/b	b_f/b	Slope* 10^{-3}
AS15	Rajaratnam and Ahmadi [26]	Asymmetric	Smooth	15.0	7.3	1.71	0.71	0.45
AS16	Macintosh [69]	Asymmetric	Rough	26.6	5.7	2.4	1.4	1
AS17	Al-Khatib and Gogus [70]	Asymmetric	Smooth	24.8	4.7	3.1	2.1	
				37.9	1.6	3.0	2.0	2.5

dataset can be categorically divided into sub-parts based on geometrical dimensions, and each dataset is given a unique code as AS1-17 (see Table 1). The number of experimental channels falls into the first category, which is not imposing, but this could be identified as the small-scale channels classified by many investigators in the past based on geometrical definitions, such as aspect ratio. Other data with medium to higher aspect ratios have fewer datasets corresponding to large-scale flume data.

The critical review of the datasets revealed that it could be interesting to experimentally explore details of flow structure and 3D flow behaviour over two differential floodplain widths. Many investigators show that the effect of wall and bed shear has a significant role in the planform vorticity and secondary circulation over the interface, especially at a lower depth. Testing these configurations will interest many researchers on the ground that the natural river often has floodplains with differential widths in real-time scenarios. Artificial channels are constructed to carry the conveyance of the flow during flood inundations [47, 48]. In the urban background, compound channels facilitate bank slope stability and higher discharge capacity for different flow rates [49]. In the river cross-section design, engineers typically consider the vegetation of the river terrace to beautify the environment and reinforce the bank soil [50, 51].

As per the study's objective, the impact of floodplains' width on the shear and mixing layer width will help to unwind the flow structures in a new asymmetric compound channel with two differential floodplains. Thus the experiments were conducted to understand turbulent structures on the floodplain with different configurations and other hydrodynamic properties like depth-averaged velocity, Reynolds shear stress, secondary currents, apparent shear stress, etc. Furthermore, for asymmetric channels, the mixing layer on the interface was estimated, and the effect of the wall was defined, for which experimental configurations from narrow floodplain to wider floodplain width were designed.

3 Experimental setup and procedure

3.1 Flume and test case condition

The experiments were conducted in the water flume at the hydraulic laboratory of Xi'an Jiaotong Liverpool University (XJTLU), which can be adjusted on a slope using a hydraulic system. The water flume facility holds two parallel channels with separate upstream and downstream control sections, and each channel is 20 m long and can be operated uninterruptedly. The cross-sections are shown in Fig. 3. The top width (B) of the channel was 0.745 m, and the total height (H) was 0.5 m. Manning's n for the single-channel bed was estimated through the depth-averaged velocity measurement over the cross-section for five discharges varying from 20 to 45 l/s. In addition, uniform flow condition is maintained by adjusting the tailgate so that the water surface slope (S_w) is kept equivalent to the bed slope ($S_o=0.003$). The point gauge (with an accuracy of 0.1 mm) installed on the traverse bridge can be moved back and forth along the channel to measure the water depth at any predetermined point.

The width ratio (B/b) in the experimental studies from the literature covers the range of 1.5 to 5.2 (Table 1). Previous studies have shown a big difference in momentum exchange for compound channels with large and small wide ratios. The cross-sectional details of new asymmetric compound channels are characterised based on a compound channel that

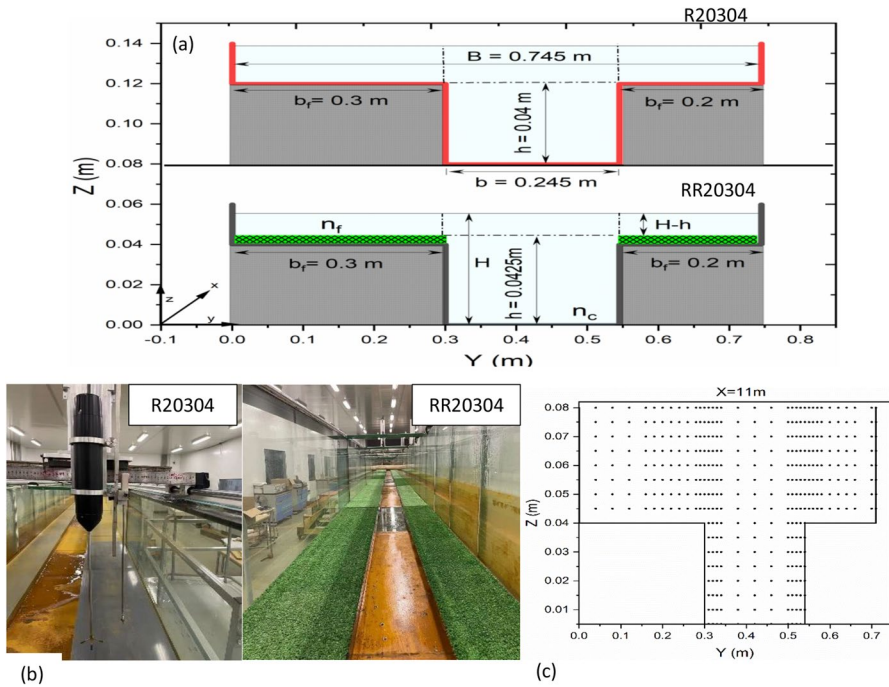


Fig. 3 **a** The cross-sectional view of the smooth (R20304) and rough (RR20304) configurations with dimensional details. **b** Picture from the downstream of the compound channel flume located at XJTU with smooth and rough floodplains having differential floodplain width, and **c** cross-sectional details of the measuring mesh points used for ADV data collection

carries the excess flow using the floodplain during high flow to avoid flood risk, as shown in Fig. 3a. The height of each test case was fixed as 4 cm and 4.25 cm for the smooth and rough main channel bankfull height, respectively. The width of the floodplain was 20 cm and 30 cm covering the width ratio (B/b) of 2.2 (R20204) and 3.04 (R20304 & RR20304), respectively. Most natural rivers have a broader floodplain to the main channel width (B/b could be up to 6.7). The aspect ratios (b/h) for the main channel bed width as 34.5 cm and 24.5 cm to the bankfull height of 4 cm and 4.25 cm were 8.625 (R20204), 6.125 (R20304), and 5.765 (RR20304), respectively. Lastly, L/B ratio, which designates the ratio of total channel length to top width, should be high enough to balance the discharge distribution between subsections and the distance required for boundary-layer development [53]. The suggested criteria of a minimum length-to-floodplain width ratio $L/b_f > 35$ could serve as a first and conservative indication for discharge distribution to reach equilibrium through mass transfer between the floodplain and main channel [54], which is maintained in the subsequent test runs.

The nomenclature's letters 'R' and 'RR' represent rectangular smooth and rough rectangular cross-sectional shapes, respectively. After 'R' and 'RR', double-digit numerals denote the width of the floodplain, which is either 20 cm or 30 cm, respectively. The last single-digit number is 4, corresponding to the bankfull height in centimetres. Note that for a channel with two different floodplain widths, each two-digit number for floodplain width was denoted one after another, following 'R' or 'RR'. For example, R20304 represents a

rectangular cross-section with a left floodplain width of 20 cm and the right floodplain width of 30 cm with a main channel bankfull height of 4 cm. The study also includes the experimental analysis of symmetric smooth channels (R20204) for comparison purposes.

3.2 Velocity measurement

Velocity measurements were conducted using Nortek micro Acoustic Doppler velocimetry. The generalised x -, y -, and z -axes refer to streamwise, transverse, and vertical (normal to bottom) directions, respectively. In this coordinate system, the instantaneous velocities, time-averaged velocities, and fluctuation velocities are denoted as (u_x, u_y, u_z) , (U_x, U_y, U_z) and (u'_x, u'_y, u'_z) respectively. Each point measurement in the cross-section was taken at the interval of 5 to 10 mm in the vertical direction and 20 to 50 mm in the lateral movement (see Fig. 3c). Near the water surface and bed, sampling was measured to the point where the instantaneous x -, y - and z -direction velocity had signal-to-noise ratio (> 15 dB) and the correlation rate within the measuring volume ($> 70\%$). Measurements were obtained by averaging time series at 200 Hz over 60–180 secs. The standard sampling errors for the critical flow parameters used in this study were estimated based on 15-time series of 600 s long each at the single measuring point. On that basis, the accuracy of ADV was ± 1 to 3% of measured mean velocities and ± 7 to 10% for Reynolds stresses. The ADV raw data were filtered in WinADV using Goring and Nikora's [55] method based on the de-spiking concept. The shortcomings of the ADV are the inability to read the upper layer velocity up to 50 mm from the free surface. To overcome the shortcomings, both side-looking and down-looking probes were used to optimally get all possible intrinsic positions in the experiments (see Fig. 3b).

The measurements were taken over the cross-section, as shown in Fig. 3c downstream at 11 m, where a uniform section was maintained by keeping the bed slope (S_o) and the water surface slope (S_w) equal through downstream tailgate settings. In general, the depth-averaged velocity data for the symmetric compound channel R20204 can be normalised with interfacial velocity ($U_{x,int}$). However, it was not easy to follow the same normalisation parameter for the cases of R20304 and RR20304 since their configurations had two interfacial velocities, i.e., the interface at 0.2 m floodplain width ($U_{x,int=0.2}$) and at 0.3 m floodplain width ($U_{x,int=0.3}$). It was either not sufficiently robust with other options of normalisation using the velocity scale U_c-U_f , where U_c and U_f are averaged streamwise main channel and floodplain velocity, respectively. For R20304 and RR20304, there are two floodplains with two consecutive overall average streamwise velocities, and therefore the overall average velocity (U_{ave}) was considered for normalisation.

4 Transverse distribution of flow quantities

4.1 The self-similar flow of symmetric and asymmetric compound channels with two floodplains

The transverse distributions of depth-averaged streamwise velocity, $U_{x,d}$, for the R20204, R20304, and RR20304 configurations are shown in Fig. 4a, b and c, respectively. The monotonic velocity profile of uniform flow conditions from shallow to deep flow regimes was observed, as discussed by researchers like Tominaga and Nezu [16] and Nezu et al. [41]. The monotonic velocity profiles with an inflexion point at the interface are associated

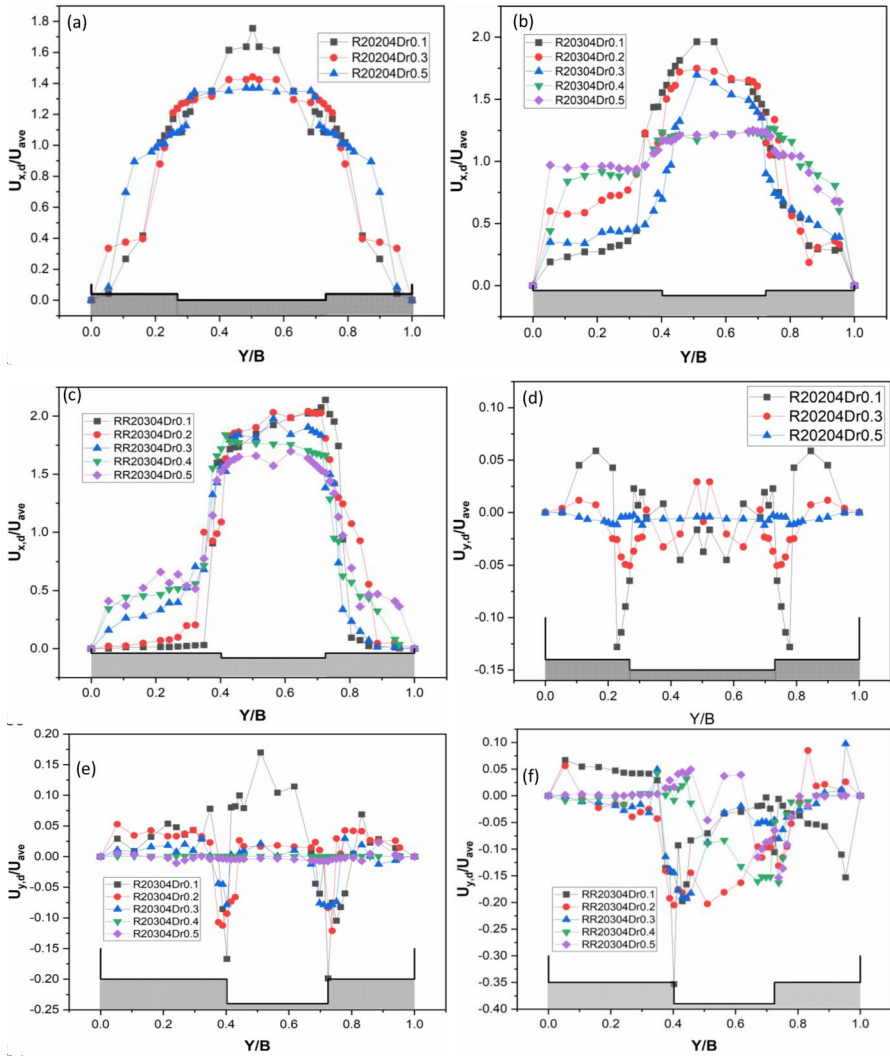


Fig. 4 Normalised depth-averaged velocity distribution over the cross-section for configurations: **a** R20204, **b** R20304, and **c** RR20304. Cross-sectional distribution of $U_{y,d}$ for the configurations are given in **d** R20204; **e** R20304; and **f** RR20304. The distribution for both the streamwise (**a–c**) and transverse (**d–f**) parameters are covered for $0.1 \leq Dr \leq 0.5$

with the large-scale vortical structures in the horizontal plane, viz., secondary currents, which have a clockwise direction towards the floodplain [16]. For particular cases, the inflexion points in Fig. 4a–c are visible at consecutive floodplain widths of 0.2 m and 0.3 m, respectively. This highlights the role of a sudden change in geometrical topography in generating these structures, as also shown in Soldini et al. [56].

In the present case of R20204 and R20304, the mean velocity distribution is strongly affected by the transverse currents, which significantly vary for differential floodplain

Table 2 Mixing shear layer width for consecutive floodplain widths of 0.2 m and 0.3 m

Test case	Dr	$\delta_{20}(m)$	$\delta_{30}(m)$
R20204	0.1	0.27	NA
	0.3	0.26	
	0.5	0.15	
R20304	0.1	0.33	0.34
	0.2	0.25	0.32
	0.3	0.26	0.30
	0.4	0.19	0.22
	0.5	0.14	0.23

width geometries in Fig. 4a and b. Note that the shear layer width change is quantified on the width of the transverse shear layer (δ) given in Eq. 1 [6].

$$\delta = 2(y_{75\%} - y_{25\%}) \quad (1)$$

The definition of δ shows the asymmetry and monotonic features of the velocity profile according to the conventional mixing length approach hypothesis. The lateral positions $y_{75\%}$ and $y_{25\%}$ respectively correspond to the positions of $\bar{U}_{y_{75\%}}$ and $\bar{U}_{y_{25\%}}$ on the profile of depth-averaged streamwise velocity. Note that $\bar{U}_{y_{25\%}} = U_f + 0.25(U_c - U_f)$ and $\bar{U}_{y_{75\%}} = U_f + 0.75(U_c - U_f)$, so the distance between the positions $y_{75\%}$ and $y_{25\%}$ determines half the mixing layer width as given in Eq. 1. The three effects of the stabilisation of the mixing layer width are defined as vertical flow confinement by Chu and Babarutsi [57], lateral flow confinement by Wood and Bradshaw [58], and the presence of the emergent roughness elements by White and Nepf [59]. Based on the experimental analysis by Dupuis et al. [4], the smooth channel was wide, and the flow was too deep compared to the length of the flume to observe stabilisation of the mixing layer width.

Table 2 depicts the shear layer width for R20304 and R20204. The value of δ would predominate the asymmetry of a shear layer for the shallow water regime ($Dr < 0.3$). The wall proximity also plays a pivotal role in this context, as shown by Dupuis et al. [4] and Proust et al. [60]. In the presence of a strong transverse current, refer to the data in Fig. 4d–f, the shear layer tends to shift towards the strong transverse current side (i.e., at the right side interface). This significant lateral displacement of the shear layer is evidence of momentum transfer via transverse currents. The shear layer width results also show that the possible width decreases over the larger floodplain side of R20304. Therefore, the wall proximity effect of the side of the channel and the vertical interfacial confinement plays a pivotal role in the dynamics of the mixing layer width. This reflects the possible increment of cross-flow momentum exchange due to transverse current near $b_f = 20$ cm, especially for $Dr \leq 0.3$ flow regimes.

Depth-averaged velocities variations in rough asymmetric compound channels with the two floodplains (RR20304) are given in Fig. 4c and f. Interestingly, the velocity distributions ($U_{x,d}$) decrease continuously from the two interfacial lines at floodplain width b_f at 0.3 m. In contrast to the channels like symmetric (two-floodplains) and asymmetric (single-floodplain), for the main channel, the maximum velocity does not happen over the centerline, which is similar to the smooth R20304 conditions (see Figs. 4a–c and 5a–e). Over the floodplain section after the inflexion point, an undisturbed and constant velocity is noticed until the position where the influence of the sidewall is ineffective [26]. The comparison of

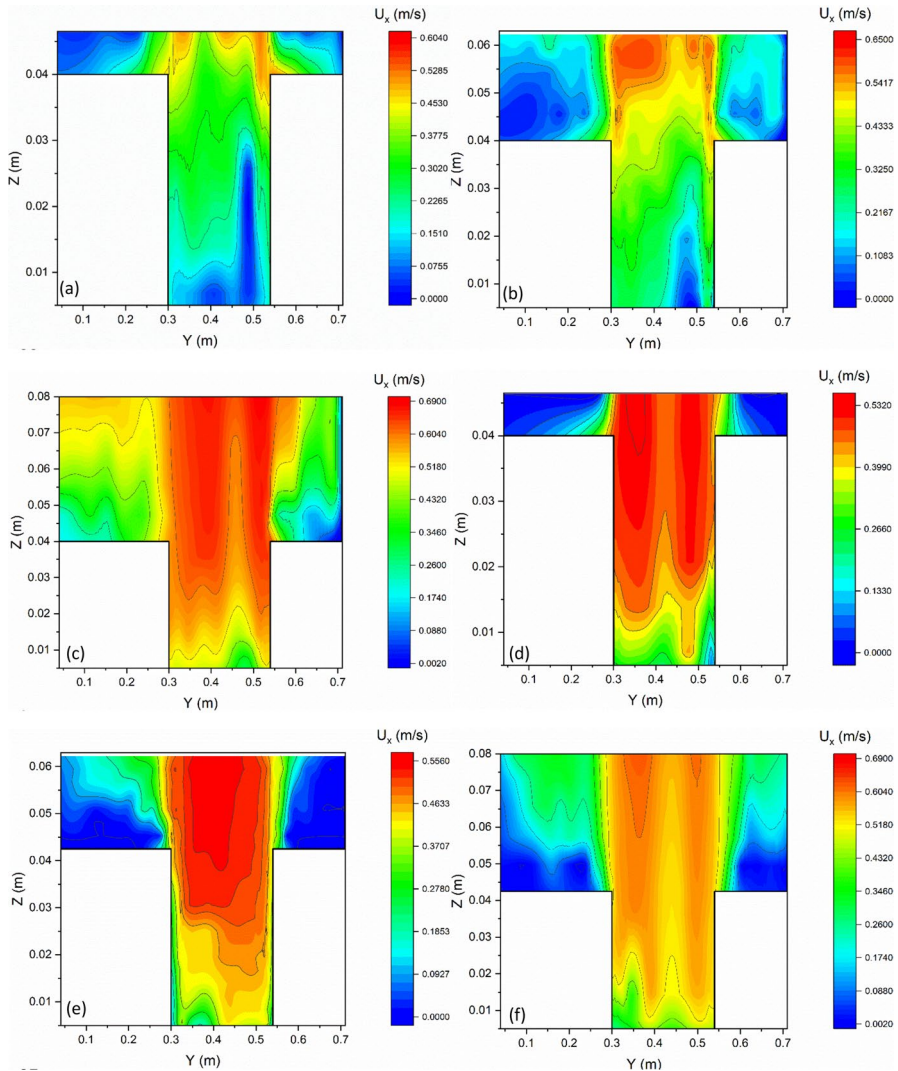


Fig. 5 Contour mapping of streamwise velocity (U_x) over the cross-section for R20304 **a–c** and RR20304 **d–f**: $Dr = 0.1$ (**a** and **d**), 0.3 (**b** and **e**) and 0.5 (**c** and **f**)

the interfacial velocity and shear layer width for R20304 and RR20304 is given in Table 3. The shear layer width in RR20304 is comparatively higher for the smaller floodplain side (δ_{20}), which is more likely because of the effect of the wall proximity and dynamics of the main-channel bulk velocity. It is evident that the shear layer expands more rapidly on the high-velocity side of the shear region than on the low-velocity side (floodplain side). Furthermore, the shear layer width is widely dissipated towards the main channel for the lower depth ratio compared to the high flow depth. This result is similar to both channels, i.e., RR20304 and R20304. Table 3 depicts a high mixing layer over the smaller floodplain. This result shows that the dynamics of the main channel shear width over 20 cm floodplain

Table 3 Mixing shear layer width for two floodplain widths of 0.2 m and 0.3 m

Test case	Dr	$U_c(m/s)$	$U_{f=0.3}(m/s)$	$U_{f=0.2}(m/s)$	$U_{ave}(m/s)$	$\delta_{30}(m)$	$\delta_{20}(m)$
RR20304	0.1	0.44	0.08	0.07	0.23	0.36	0.37
	0.2	0.47	0.14	0.09	0.24	0.33	0.37
	0.3	0.50	0.18	0.14	0.26	0.32	0.36
	0.4	0.57	0.26	0.19	0.33	0.31	0.38
	0.5	0.60	0.28	0.28	0.37	0.32	0.32
R20304	0.1	0.32	0.09	0.08	0.19	0.34	0.33
	0.2	0.46	0.16	0.13	0.27	0.32	0.25
	0.3	0.47	0.21	0.14	0.29	0.30	0.26
	0.4	0.59	0.42	0.39	0.49	0.22	0.19
	0.5	0.61	0.45	0.35	0.51	0.23	0.14

is strongly influenced and driven by the main channel and floodplain width interaction in cases like R20304, which is driven by the main channel geometry.

Figure 5a–c shows the contour mapping of R20304 for three depth ratios $Dr = 0.1, 0.3,$ and 0.5 , except for $Dr = 0.2$ and 0.4 , where only the depth-averaged values were measured. The distribution of the contour mapping depicts that the maximum velocity tends to appear below the free surface in the main channel ($0.3 \leq Y \leq 0.545$), which is not found to be equally distributed in the main channel compared to the symmetric compound channels shown by previous investigators [61]. In Fig. 5a–c, the deceleration due to low momentum transport from the interfacial junction edge extends to the free surface. The primary mean velocity structure is affected by the momentum transport of the secondary current and Reynolds stress, which seems imbalanced over the floodplain width of 0.2 and 0.3 m. Figure 5d–f shows contour mapping for streamwise velocity distribution for RR20304 at three depth ratios. The dark blue region over the floodplains depicts a small velocity near the bed for RR20304, which is evident because of the higher roughness than R20304. It is also visible that the maximum velocity beneath the free surface is shifted over the sections of the channels.

4.2 Depth-averaged Reynolds stress

The normalised Reynolds shear stress ($-\overline{u'_x u'_y}$) is given in Fig. 6a–c for R20204, R20304, and RR20304, respectively. In addition, Fig. 7 shows contour mapping of the lateral Reynolds stresses $\overline{\rho u'_x u'_y}$ for three depth ratios: $Dr = 0.1, 0.3$ and 0.5 for R20304 and RR20304. The results clearly show that the Reynolds stress reaches the maximum at the interface for compound channels, irrespective of configurations. Within the lateral shear zone, the highest values of the $\overline{\rho u'_x u'_y}$ are generally near the junctions, as seen in Fig. 7.

The peak of the Reynolds shear occurs at the lower depth ratio ($Dr = 0.1$). The negative values of the $\overline{\rho u'_x u'_y}$ are near the interface and mainly around the shear layer width (Fig. 7). These negative Reynolds stress values are dominant in a lower depth ratio case. However, it is interesting that these peaks of Reynolds stress ($-\overline{u'_x u'_y}$) at interface do not show symmetry for R20304 (see Fig. 6b and c for distinct differences). The value for the $-\overline{u'_x u'_y} / U_{ave}^2$ for R20304 in lower depth ratios (Dr) is comparatively higher on the interfacial side than R20204 (Fig. 6a and b). This high value signifies a higher shear layer based on the bulk velocity difference over the sub-sections.

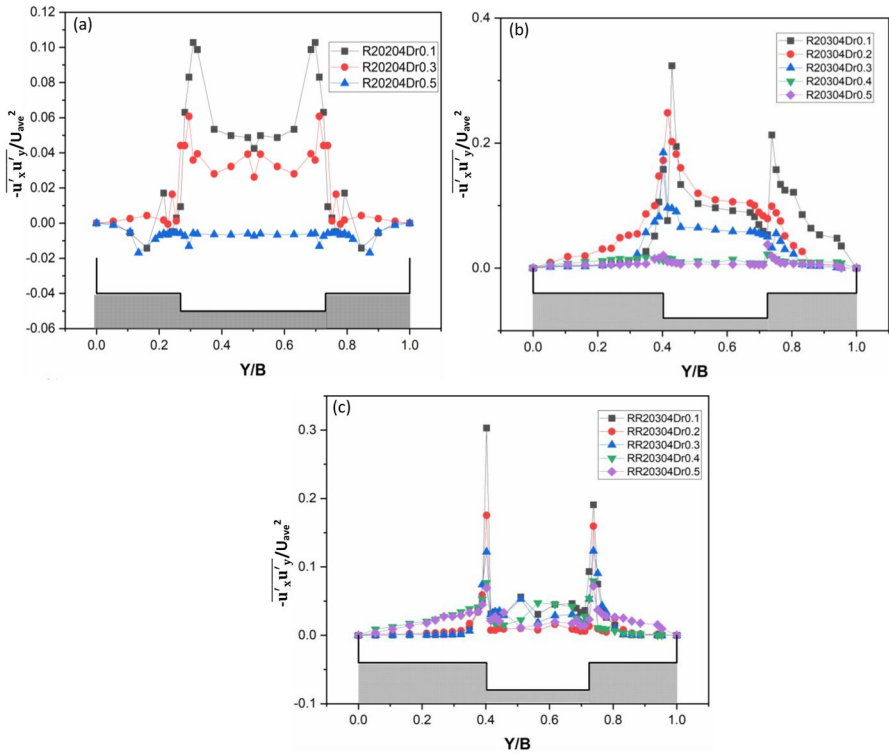


Fig. 6 Cross-sectional distribution of the dimensionless transverse Reynolds shear stress for configurations **a** R20204, **b** R20304, and **c** RR20304, respectively

In particular, to the rectangular asymmetric smooth channels of the differential floodplain widths (R20304), the higher peak values of the $-\overline{u'_x u'_y} / U_{ave}^2$ are observed in the large floodplain width side $b_f = 0.3$ m for $Dr = 0.1$. Moreover, this result trend aligns with other depth ratios, except $Dr = 0.1$. In the floodplain(s), the values of $-\overline{\rho u'_x u'_y}$ are negative, adjacent to the interface, and evident on the bankfull side ($h = 0.04$ m) (Fig. 7). This result happens because the turbulence intensity increases near the bed, defined as a bed and wall-influenced turbulence. On the main channel, $-\overline{\rho u'_x u'_y}$ are mostly positive, except near the bed, which shows bed-induced shear. The negative value over the interfacial region illustrates the turbulent diffusion of high-momentum fluid from the main channel to the floodplain. These values are visibly different for the different floodplain widths of asymmetric channel R20304, which is essential in identifying the momentum transport difference.

On the other hand, the negative region of the $-\overline{\rho u'_x u'_y}$ corresponds to the negative gradient of the mean velocity in the vertical direction. The value of the Reynolds shear increases just above the junction edge, where the adjacent negative region gets hyped and is visible in Fig. 7d–f. Over the floodplain side, the distribution is linear or bulges towards the junction and contracts near-wall proximity. This phenomenon is well prominent over the floodplain side of the 0.3 m width. The differential positive and negative values of the Reynolds shear over floodplain(s) and the main channel imply the existence of momentum transport.

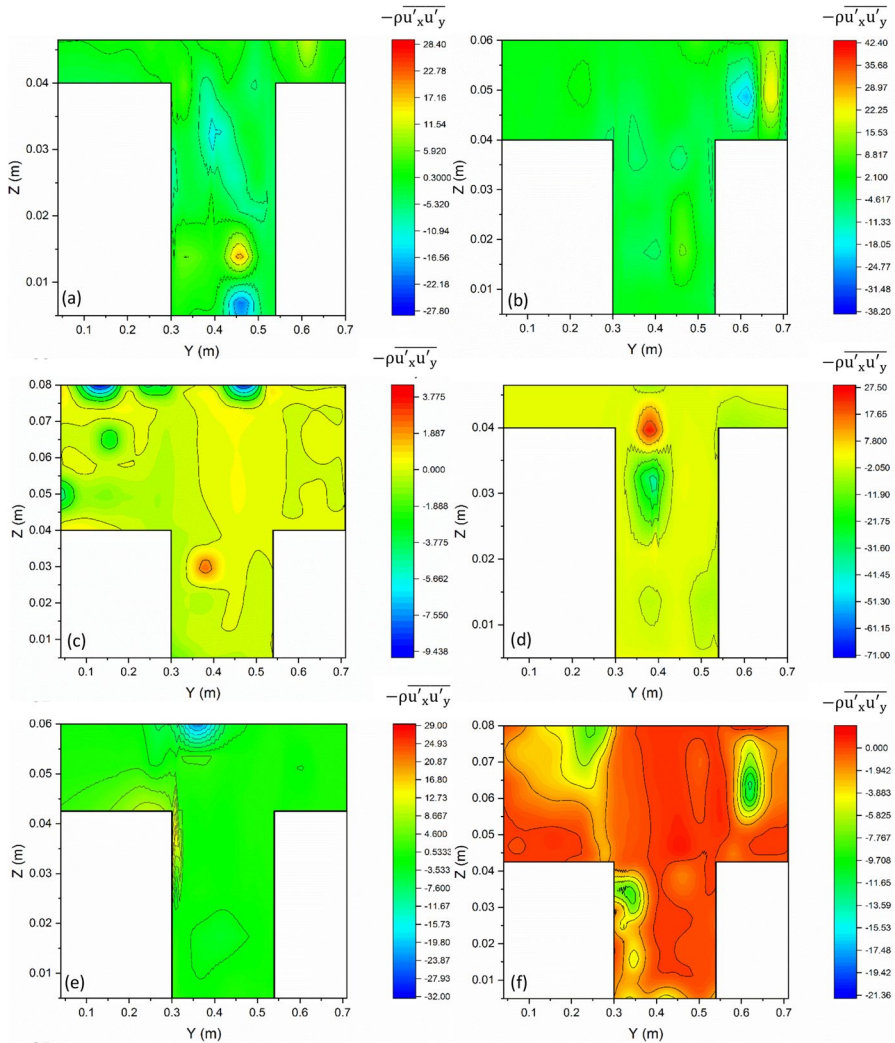


Fig. 7 The contour of the lateral Reynolds stress ($-\overline{\rho u'_x u'_y}$) in N/m^2 for **a–c** R20304 and **d–f** RR20304: $Dr = 0.1$ **a–d**, 0.3 **b** and **e** and 0.5 (**c** and **f**)

4.3 Turbulence intensities

Lateral distributions of the normalised turbulent intensities ($\overline{u'^2}$) for R20204, R20304, and RR20304 are presented in Fig. 8a–c. The cross-sectional distribution of the contour map of the transverse ($\overline{\rho u'^2}$) and streamwise ($\overline{\rho u'^2}$) turbulence intensities are shown in Figs. 9 and 10a–c R20304 and d–f RR20304 for three depth ratios: $Dr=0.1, 0.3$ and 0.5 . The magnitudes of the peak turbulence intensities concentrate in the interfacial region, i.e., the peak position in the spike is at the interface section. Furthermore, the difference between the turbulence intensities is less important over the main channel region and near the sidewall of the floodplain(s). The variation of the turbulence is mostly attributed to the flow depth effect

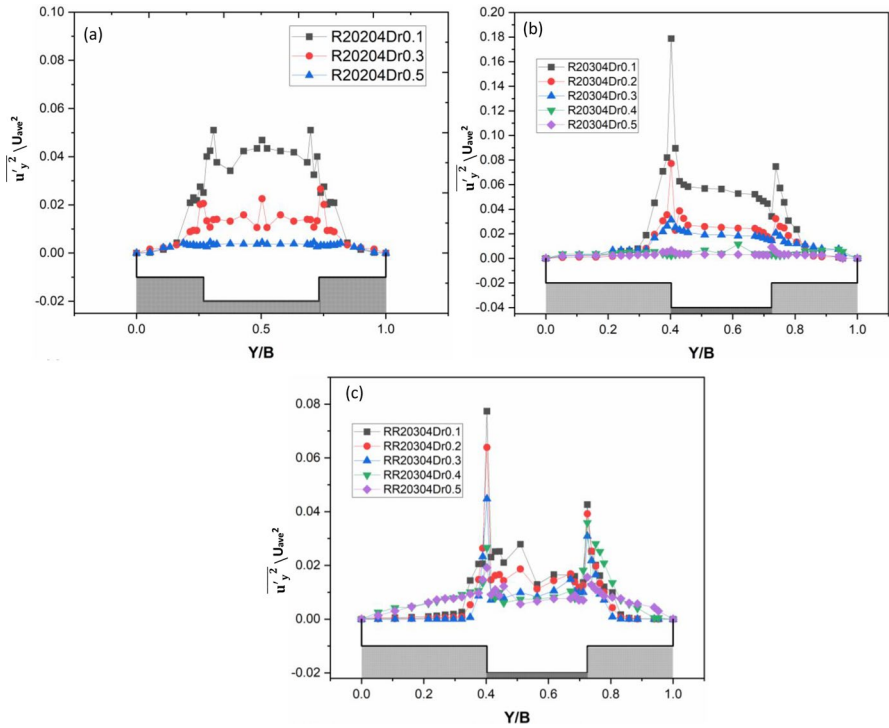


Fig. 8 Cross-sectional distribution of the dimensionless transverse squared turbulence intensity for configurations **a** R20204, **b** R20304 and **c** RR20304, respectively

on the floodplain(s). Due to the high bed-induced turbulence in the shallow flow regime, the energy budget varies from the bottom to the free surface (Figs. 9 and 10a, b, d and e).

From a comparative standpoint, turbulence statistics over the interface between R20304 and RR20304 are shown in Table 4. The width size identifies the two interfaces (b_f) as 0.3 m and 0.2 m. The turbulence level from the streamwise intensities is higher on the smaller floodplain width side ($b_f = 0.2$ m). However, the transverse turbulence intensity is higher on the floodplain side of the larger width ($b_f = 0.3$ m). This result indicates that the primary source of turbulence on the more extensive floodplain is the momentum transport and mixing layer, which creates a high lateral turbulence intensity around the large floodplain side. Furthermore, this particular phenomenon is enhanced with an increasing depth ratio. For a higher depth ratio, both the turbulence intensities ($u'_y{}^2$ and $u'_x{}^2$) are sublimed and have the same magnitude. These sources of turbulence for the higher depth ratio are the boundary layer induced by the sidewall and bottom, which diffuses towards the free surface (also refer to Figs. 9e and 10 f). Reynolds stress is higher in the $b_f = 0.3$ m sides, and the magnitude of $-u'_x u'_y$ is sizeably different for the lower depth ratio. Similarly, the higher depth ratio has a similar magnitude on both sides of the floodplains.

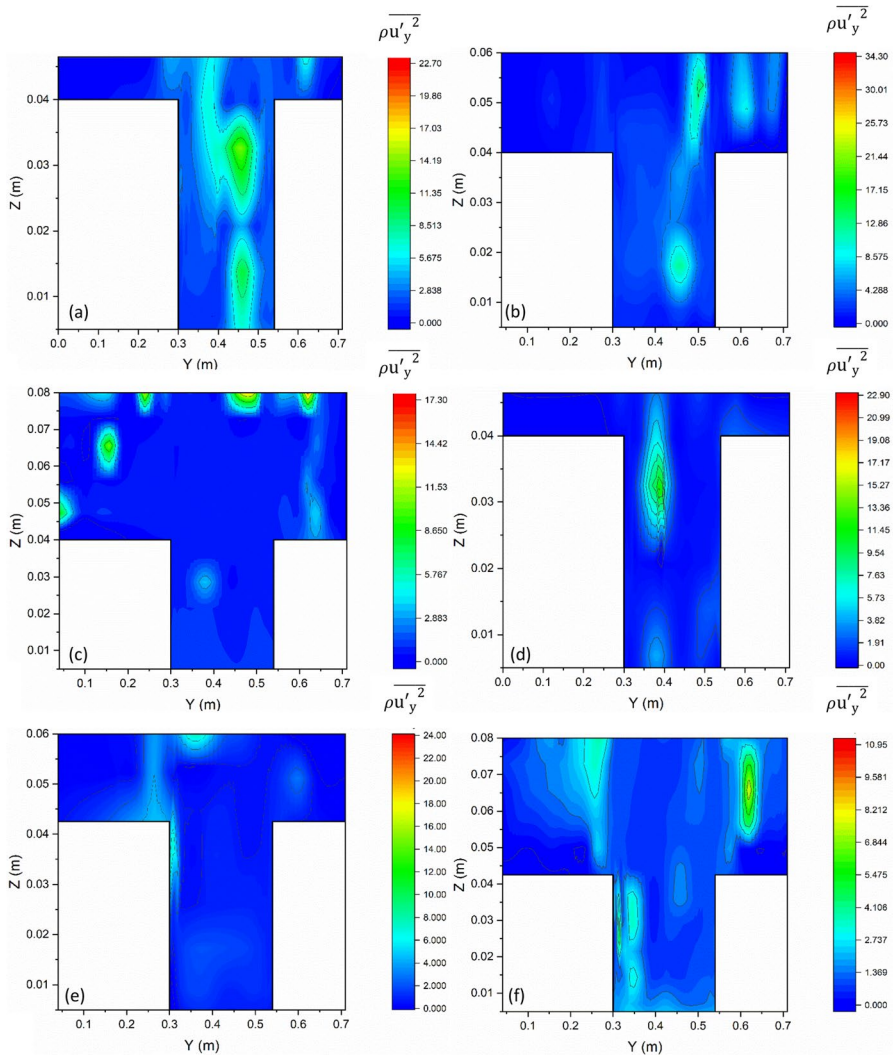


Fig. 9 The contour plots of the lateral turbulence intensity ($\overline{\rho u'^2}$) in N/m^2 for **a–c** R20304 and **d–f** RR20304: $Dr = 0.1$ (**a** and **d**), 0.3 (**b** and **e**) and 0.5 (**c** and **f**)

5 Effect of coherent structures

5.1 Power spectral density and quadrant analysis over two interfaces

A power spectral density (PSD) and quadrant analysis are practical turbulence data processing methods to provide an insightful understanding of the turbulent shear stress from various events of flows [62–64]. Figure 11a and b illustrates the PSD of the transverse fluctuating velocity at the bankfull height of the interfaces at $b_f = 0.3$ m and $b_f = 0.2$ m for R20304 and RR20304, respectively. It is visible in both cases that at

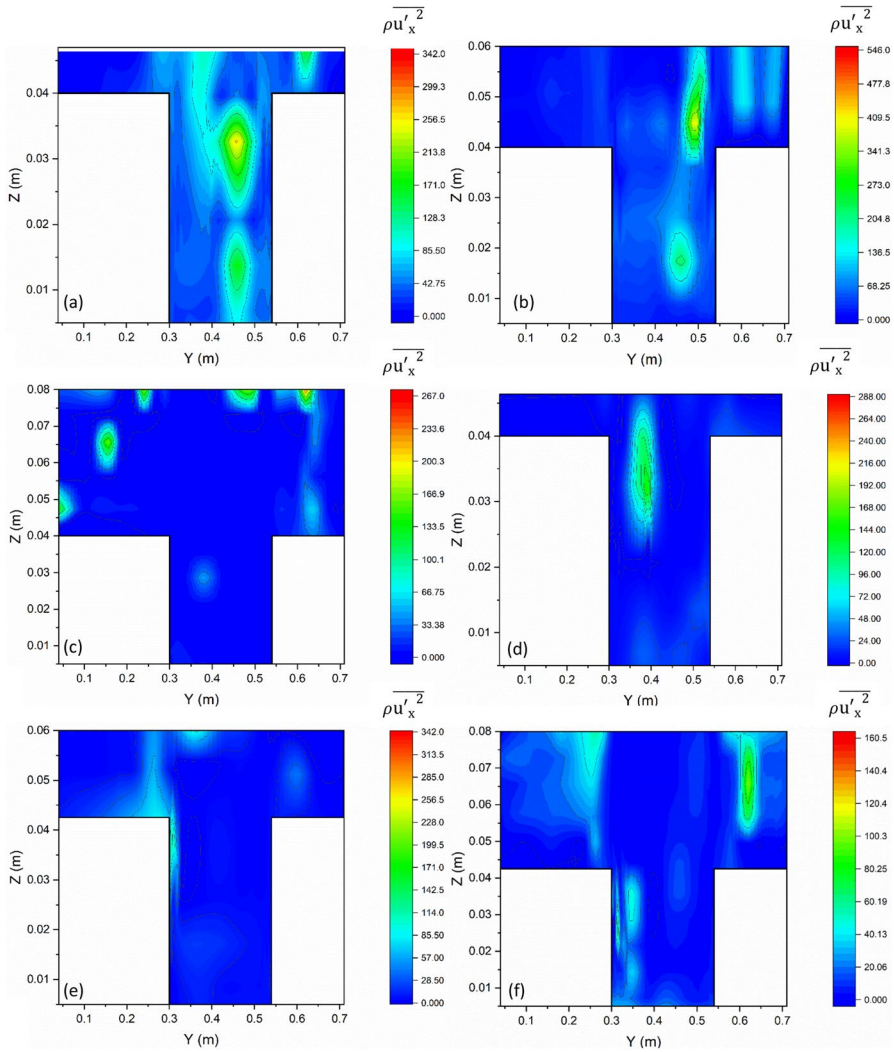


Fig. 10 The contour of the lateral turbulence intensity $(\overline{\rho u_x'^2})$ in N/m^2 for **a–c** R20304 and **d–f** RR20304: $Dr = 0.1$ (**a** and **d**), 0.3 (**b** and **e**) and 0.5 (**c** and **f**)

the high-frequency region of the PSDs, the decrease in energy density almost follows a slope of $-5/3$, which is indicative of flows with a sizeable inertial subrange. The low-frequency analysis on PSD of the transverse velocity fluctuation has no significant peaks to relay quasi-2-D large horizontal coherent structures. Thus, Reynolds shear stress induces coherent structures (low-frequency signals) that cannot be compared with the total Reynolds shear stresses over interfaces in these cases. Predominantly, the results from Fig. 11a and b confirm that the coherent structures' contribution to the total turbulent shear stress is present across the interfaces of differential width or the R20304 and RR20304 channels. However, large-scale coherent structures to small-scale motions in the flow are correlated differently, reducing Reynolds shear stress induced by large-scale motions.

Table 4 The normalised peak value of the Reynold stress ($-\overline{u'_x u'_y} / U_{ave}^2$), turbulent intensity in longitudinal ($\overline{u'^2} / U_{ave}^2$) and transverse direction ($\overline{v'^2} / U_{ave}^2$) at the main channel and floodplain interface for smooth and rough asymmetric channels with two differential width floodplain(s)

Configurations	D_r	$\overline{u'^2} / U_{ave}^2$		$\overline{v'^2} / U_{ave}^2$		$-\overline{u'_x u'_y} / U_{ave}^2$	
		$b_f=0.3$	$b_f=0.2$	$b_f=0.3$	$b_f=0.2$	$b_f=0.3$	$b_f=0.2$
R20304	0.1	0.7358	0.2149	0.0463	0.0194	0.0893	0.0554
	0.2	0.1058	0.1997	0.0253	0.0106	0.0517	0.0324
	0.3	0.1454	0.3358	0.0110	0.0072	0.0397	0.0491
	0.4	0.0431	0.0791	0.0034	0.0046	0.0106	0.0112
	0.5	0.0407	0.0426	0.0042	0.0035	0.0130	0.0123
RR20304	0.1	0.2591	0.3155	0.0773	0.0252	0.0661	0.0416
	0.2	0.1155	0.2421	0.0639	0.0253	0.0421	0.0383
	0.3	0.0850	0.1789	0.0448	0.0218	0.0312	0.0315
	0.4	0.0655	0.1490	0.0267	0.0281	0.0227	0.0235
	0.5	0.0870	0.1410	0.0192	0.0127	0.0241	0.0249

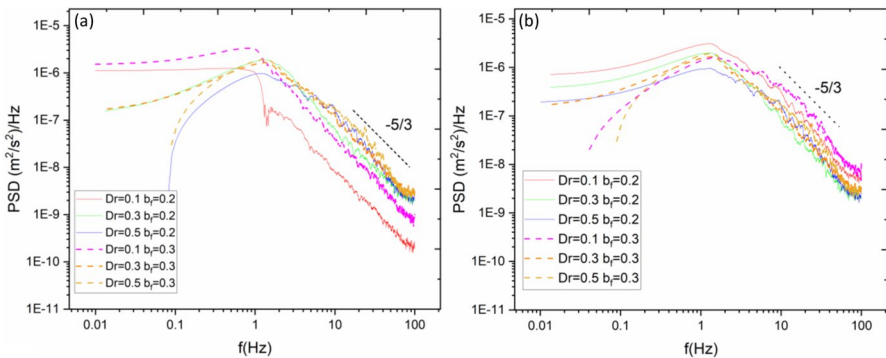


Fig. 11 Representative power spectral density at the interface of the main channel and floodplain width side of $b_f = 0.3$ m and $b_f = 0.2$ m for different depth ratios for **a** R20304 and **b** RR20304 configurations

A quadrant analysis at the exact location of the interface will shed more light on the structures induced at different floodplains of the asymmetric compound channels. Figure 12 shows the results of the four quadrants associatively depicting various events happening at different interface locations of the R20304 and RR20304 configurations for $Dr = 0.5$. By definition, quadrant analysis involves streamwise and transverse fluctuating velocity components to illustrate events related to the outward interaction ($u'_x > 0, u'_y > 0$), ejections ($u'_x < 0, u'_y > 0$), inward interaction ($u'_x < 0, u'_y < 0$), and sweeps ($u'_x > 0, u'_y < 0$). According to the sign of u'_x and u'_y , the quadrant analysis divides the RSS into four quadrants (I-Q1, II-Q2, III-Q3, and IV-Q4). These four quadrants are associated with four events: outward interactions, ejections, inward interactions, and sweeps.

Figure 12 shows that $S_{i,H}$ is negative for outward and inward interactions ($i = 1, 3$) and is positive for ejections and sweeps ($i = 2, 4$). H is the parameter defined by the hyperbolic hole region, which allows the investigation of a more considerable contribution to the total Reynolds shear stress from various quadrants. This analysis considers $H=0$, implying that

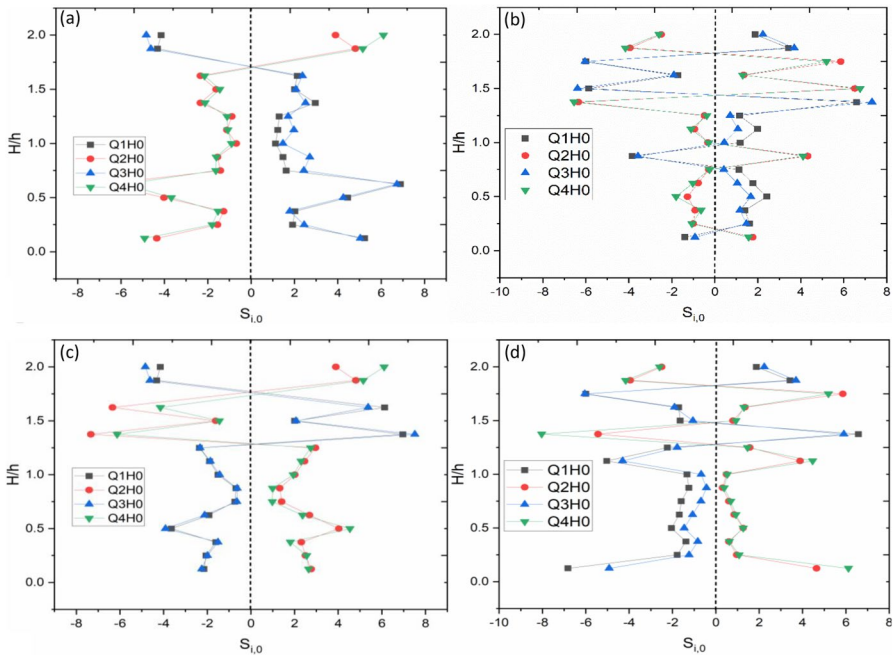


Fig. 12 The quadrant analysis using measured (u'_x) and (u'_y) at locations **a** and **c** $b_f = 0.2$ m (at the smaller floodplain interface), $H=0$ (**a**); and **b** and **d** $b_f = 0.3$ m, $H=0$ (at the larger floodplain interface) in the main open channel for $Dr = 0.5$ of (**a** and **b**) R20304 and (**c** and **d**) RR20304, respectively. Q1, Q2, Q3, Q4 velocity-intensity quadrants

hole size disappears. Figure 12a and b indicates that the quadrant of flow events in both configurations, associated with the large-scale coherent structures, is visible over the bankfull height. At the edge of the floodplain(s) $b_f = 0.3$ m and $b_f = 0.2$ m, the distribution of (u'_x, u'_y) corresponding to the bursting events is prominently found in all four events (Q1–Q4). Indicatively, the occurrence of these events over the bankfull height suggests that the passage of the structure strongly influences flow behaviour. The momentum exchange happens strongly at the interface of the floodplain(s), mediated by Q2 and Q4. Irrespective of this generalised behaviour, the difference in quadrant analysed events at the two separate interfaces at $b_f = 0.3$ m and $b_f = 0.2$ m have the same behaviour indicating the momentum transfer due to the 'large' coherent structures in the same order for both interfaces.

6 Flow interaction between the main channel and floodplain(s)

For all the test cases, the shear layer turbulence, transverse currents, and secondary currents contribute to the depth-averaged transverse exchange of streamwise momentum. Figure 13a–c shows the lateral distribution of apparent shear stress (τ_a) at the three depths of the channels constituting symmetric and asymmetric floodplain(s). Equation (2) defines the apparent shear stress based on three momentum mechanism components: transverse Reynolds stresses, transverse currents and secondary current on the right-hand side, respectively. The effect of the turbulent exchange on the interface is visible in Fig. 13a–c for the

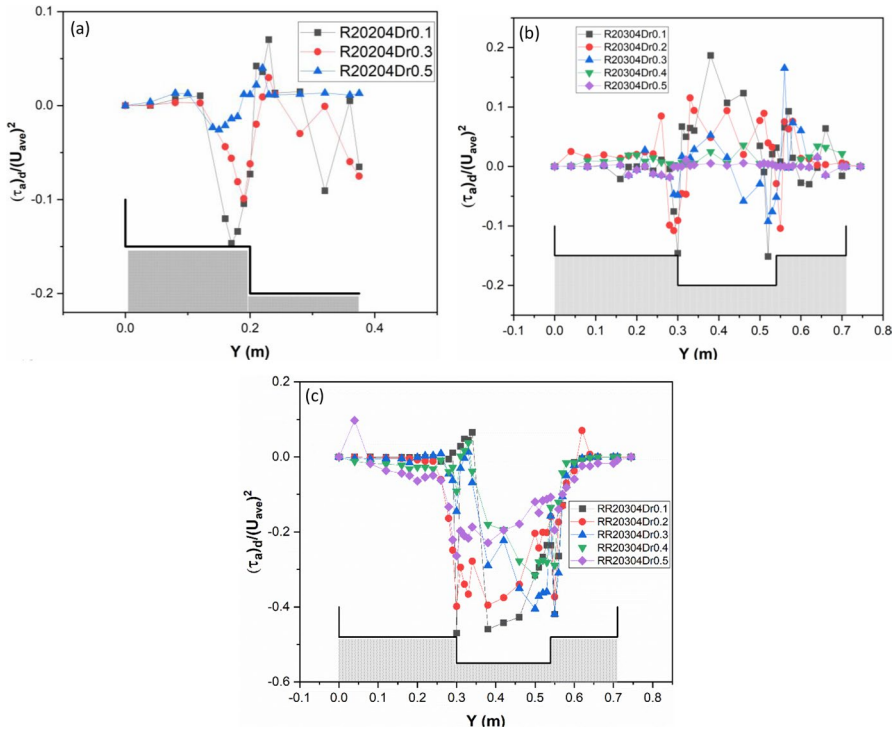


Fig. 13 Spanwise distribution of apparent shear stress τ_a for the configurations: **a** R20204; and **b** R20304 and **c** RR20304

low-depth ratios. It is well established that the impact of the shear layer (planform) turbulence and transverse currents have similar magnitudes in the depth-averaged momentum exchange, while the effect of the secondary currents is negligible [4, 6, 60]. The $U_{y,d}$ over the interface for the low depth ratio peaks at the interface but has a minimal magnitude, which is 6–10% of the mean streamwise velocity ($U_{x,d}$).

$$(\tau_a)_d = \frac{1}{H} \int_0^H \rho u_x u_y dz = -\rho \overline{(u'_x u'_y)}_d - \rho U_{xd} U_{yd} - \rho [U_x (U_y - U_{yd})]_d \quad (2)$$

The apparent shear stress in R20304 is comparatively higher than in R20204, which could be explained because the shear layer development significantly contributes to the redistribution of momentum. Figure 13c shows the transverse exchange of streamwise momentum defined as apparent shear stress in RR20304. It is evident in RR20304 that the momentum fluxes by the Reynolds stress and the transverse currents have the same sign, which signifies the flow acceleration towards the floodplain. Moreover, the apparent shear stress result shows a higher magnitude in the rough asymmetric compound channels with two differential floodplains (see Fig. 13c). The higher value of the apparent shear stress in the main channel is highly influenced by the shear layer turbulence and does not influence the Reynolds stress and secondary currents. Furthermore, the higher magnitude of the apparent shear shooting in the main channel near the small floodplain $b_f = 0.2m$ can be explained due to the higher planform shear layer influence (see Table 4).

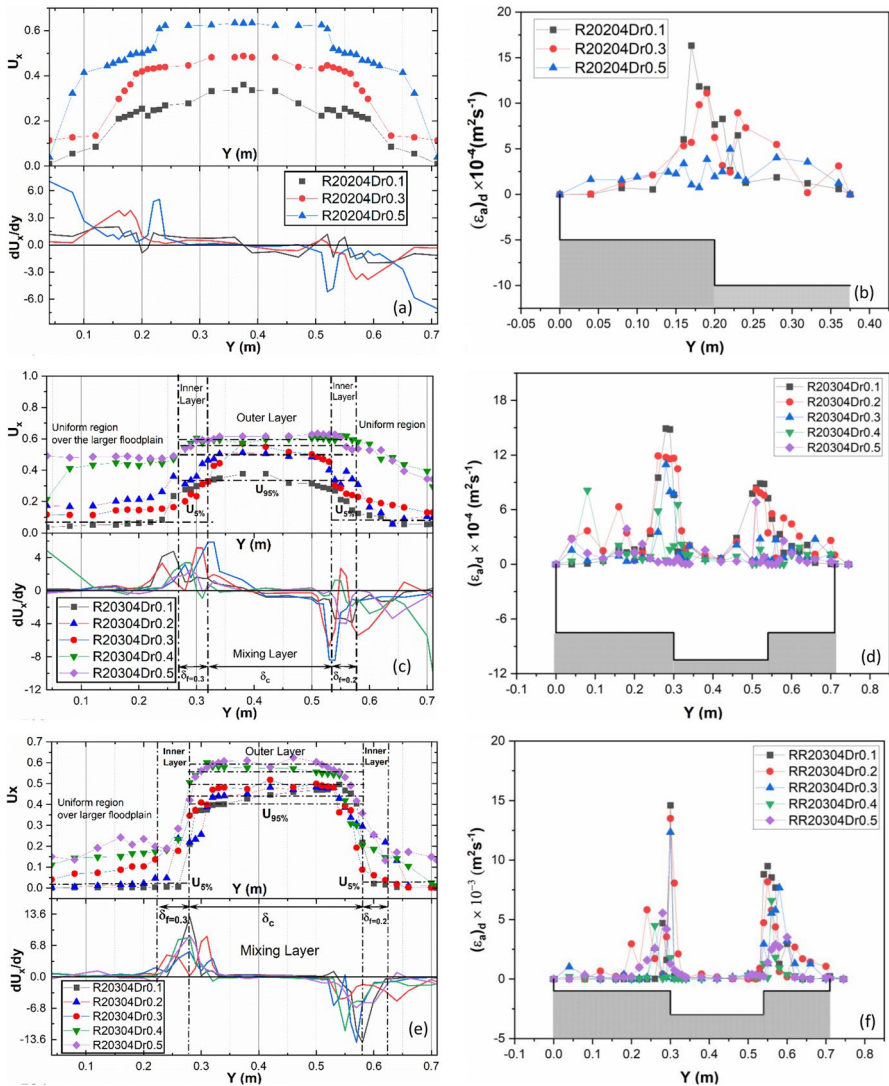


Fig. 14 Representative mean streamwise velocity profile, the streamwise gradient of flow and eddy viscosity profile determined according to the viscosity model as per the definition of model the turbulent shear stress for **a, b** R20204, **c, d** R20304 and **e, f** RR20304

6.1 Eddy viscosity at the interface of the main channel and floodplain(s)

The eddy viscosity concept or Boussinesq approach is used to model the turbulent shear stress ($\overline{\tau}_{ad} = \epsilon_a \frac{dU_x}{dy}$). Figure 14a, c, and e shows the first derivative of the transverse distribution of depth-averaged streamwise velocity. Accordingly, the determination of the transverse exchange of momentum is replaced by a proper eddy viscosity model like the effective eddy viscosity concept of van Prooijen et al. [6], the vortex-based model of White and Nepf [65], Tamai et al. [66], Uijtewaal and Booji [24], Knight et al. [67], Xiaohui and Li

[68], etc. It is evident from Fig. 14b, d and f that eddy viscosity peaks are seen over interfaces, irrespective of the channel types. However, a comparatively small peak is visible for the higher depth ratio of $0.3 < Dr \leq 0.5$. The role of the water depth ratio (Dr) has been acknowledged as it is associated with an increased shear rate and the consequent appearance of coherent structures [41, 67].

The qualitative link between the gradient of flow ($\frac{d\bar{U}_x}{dy}$) and the lateral shear stress illustrates that the mass transferred to the floodplain induces a substantial increase in eddy viscosity (ε_a). Hence, these profiles in Fig. 14b, c and f highlight the interaction between the transverse flow and the shear layer turbulence. Furthermore, the gradient of streamwise flow over the differential floodplain widths of R20304 and RR20304 is not symmetric as found in R20204 conditions (refer to Fig. 14a, c and e). The sharp spike in the flow gradient over the interface of the main channel and floodplain(s) corresponds to inflexion in the velocity profile, which implies the shallower floodplain(s) effect. By another definition by Truong and Uijtewaal [71] for δ different from Eq. 1, the mixing layer for penetration can be divided into two layers, corresponding to the penetration layer and the outer layer: $\delta = \delta_{f=0.3} + \delta_c + \delta_{f=0.2}$ (Fig. 14c and e). The penetration width of the mixing layer into the grass-roughened floodplain is defined as the distance required for the flow velocity to achieve a constant value inside the floodplain (U_f) plus an error of 5%. In other words, the penetration is the distance from the position where the mean streamwise velocity is 5% different from the uniform mean streamwise velocity further inside the floodplain (U_f) to the roughened floodplain edge: $\delta_{f=0.3\&0.2} = y_0 - y_{5\%}$ and $U_{5\%} = U_{f=0.3\&0.2} + 0.05U_{f=0.3\&0.2}$. A similar rule is also applied for the outer layer width: $\delta_c = y_{95\%} - y_0$ and $U_{95\%} = U_c - 0.05U_c$. From the above definition, it is evident that the mixing layer penetration for the asymmetric compound open channel with differential floodplain width (Fig. 14c and e) varies over the floodplain width side $b_f = 0.3$ m and $b_f = 0.2$ m. Furthermore, the mixing layer penetration, dependent on the size of the floodplain width, is prominently dispersing to the main channel since the difference in bulk velocity over two sections is higher in rough channels.

6.2 Momentum flux distribution at the vertical interface

The three attributing variables of the transverse momentum flux are $U_{x,d}U_{y,d}$, $\overline{u'_x u'_y}$ and $\overline{u'_x}(\overline{u_y} - U_y)|_d$, where the transverse velocity $\overline{u_y}$ plays a significant role. The vertical distributions of velocity U_y , Reynolds shear stress (RSS), $\overline{u'_x u'_y}$, and anisotropy are shown in Fig. 15a–f at the interface of the main channel having differential floodplain width side $b_f = 0.3$ m and $b_f = 0.2$ m. The degree of flow anisotropy is measured by the ratio of σ_z/σ_x , where, $\sigma_z = \sqrt{\overline{u'_z u'_z}}$ and $\sigma_x = \sqrt{\overline{u'_x u'_x}}$ are the standard deviations of the vertical and streamwise velocities, respectively. Near the vertical interface of the configurations R20304 and RR20304 and inside the shear layer, the magnitude of the transverse velocity and RSS is in the same order for a higher depth ratio. However, for the lower depth ratios, the peaks of the U_y , $\overline{u'_x u'_y}$, and anisotropy is located at the bankfull height of the main channel, but for higher depths, these peaks move towards the free surface, irrespective of the channel configurations. In the shear layer, the momentum is essentially driven by the time-averaged $\overline{u'_x u'_y}$ in the RR20304 configuration (see Fig. 15d). Figure 15a and b shows that the overall shape of the U_y profile has a more significant spike at the bankfull edge of the main channel for the more expansive floodplains $b_f = 0.3$ m. The presence of anisotropy above the bankfull height in Fig. 15e and f illustrates the lateral displacement of the same order towards the floodplain(s).

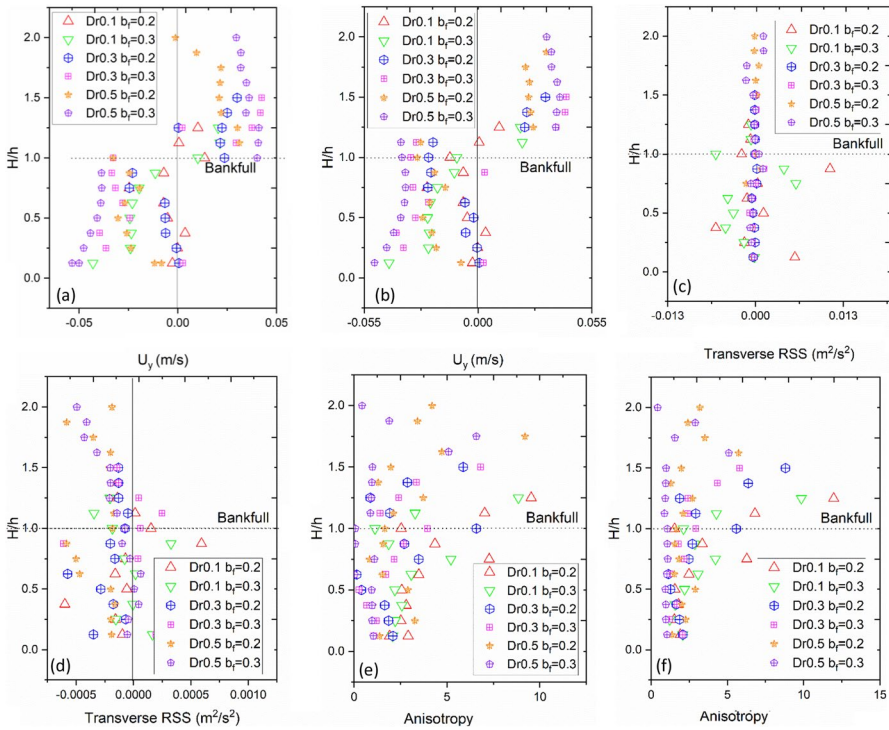


Fig. 15 Vertical distribution of **a** and **b** transverse velocity, **c** and **d** Reynolds shear stress ($RSS \overline{u'_x u'_y}$) and **e** and **f** anisotropy over the interface in the main channel of **(a, c, and e)** R20304 and **(b, d, and f)** RR20304 configurations

6.3 Conclusions

A straight asymmetric and one symmetric compound channel configurations have been experimentally investigated in the experimental study conducted to understand the mixing length at different interfaces of the compound open channels. For the cases of smooth symmetric (R20204) and asymmetric (R20304) channels with two floodplains, the mean velocity distribution is strongly affected by the transverse currents, which significantly vary for differential floodplain width geometries. By analysing the experimental result of R20304, it becomes evident that vertical confinement plays a vital role in understanding the dynamics of the mixing layer width. The cross-flow momentum exchange due to transverse current near the smaller floodplain has a prominent increment for shallow flow regimes. In the case of the rough asymmetric compound channels with two different-sized floodplains (RR20304), maximum velocity does not appear over the channel’s centerline. Comparing the interfacial velocities between RR20304 and R20304 shows that the velocity transition is smoother over the larger floodplain width than the smaller floodplain.

In common for all the configurations, a local maximum of turbulence intensity and lateral Reynolds shear values can be observed at the interfacial junction of the main channel and floodplain(s). The spike in the turbulence intensity and lateral Reynolds shear stress for R20304 and RR20304 is no longer symmetric compared to R20204. Regarding the stream-wise turbulent intensity, the turbulence level is higher on the smaller floodplain width.

However, the transverse turbulence intensity is higher for the larger floodplain width in the cases of R20304 and RR20304. The pattern of the lateral turbulence intensity near the interface shows a strong anisotropy of the turbulence, consequently becoming the critical factor of the secondary current generation.

The momentum flux at the interface is due to the anisotropy of the planform shear layer turbulence. A strong transverse current shifts the shear layer, evident in the R20304 and RR20304 configurations. The strong transverse current on the larger floodplain side in R20304 and RR20304 shows a significant shift in the shear layer. The apparent shear stress and eddy viscosity for the asymmetric compound channels with two floodplains (R20304) have a higher magnitude than the symmetric compound channel (R20204), which the higher redistribution of momentum over differential floodplain width could explain. In RR20304, the main channel is highly influenced by the shear layer turbulence from two different-width floodplains. Furthermore, a higher magnitude of the apparent shear stress shooting at the smaller floodplain width is due to higher planform shear layer influence. The 3D flow structures analysis through PSD and quadrant analysis shows that the large coherent structures indifferently affect the Reynolds shear stress distribution to interfaces of the floodplains of variable widths.

Acknowledgements The authors would like to acknowledge the National Natural Science Foundation of China (11772270) and the research funding of XJTLU (REF-20-02-03 and PGRS2012007). Furthermore, the authors would also like to sincerely thank all the past researchers who gave valuable experimental datasets.

Author's contribution PS: Conceptualization, Investigation, Methodology, Formal analysis, Writing—original draft. XT: Conceptualization, Methodology, Supervision, Editing and Review, Funding acquisition, HI: Formal analysis, Editing and Review.

Funding This work was supported by the Grants National Natural Science Foundation of China (11772270) and the research funding of XJTLU (REF-20-02-03 and PGRS2012007).

Data availability The corresponding author will avail the data on request.

Declarations

Conflict of interest The authors declare that they have no known competing financial interests or personal relationships that could have influenced the work reported in this paper.

References

1. Knight DW, Shiono K (1990) Turbulence measurements in a shear layer region of a compound channel. *J Hydraul Res* 28(2):175–196
2. Nezu I, Nakayama T (1997) Space-time correlation structures of horizontal coherent vortices in compound open-channel flows by using particle-tracking velocimetry. *J Hydraul Res* 35(2):191–208
3. Proust S, Fernandes JN, Leal JB, Rivière N, Peltier Y (2017) Mixing layer and coherent structures in compound channel flows: effects of transverse flow, velocity ratio, and vertical confinement. *Water Resour Res* 53(4):3387–3406
4. Dupuis V, Proust S, Berni C, Paquier A (2017) Mixing layer development in compound channel flows with submerged and emergent rigid vegetation over the floodplains. *Exp Fluids* 58(4):1–18
5. Bousmar D, Riviere N, Proust S, Paquier A, Morel R, Zech Y (2005) Upstream discharge distribution in compound-channel flumes. *J Hydraul Eng* 131(5):408
6. Van Prooijen BC, Battjes JA, Uijttewaals WS (2005) Momentum exchange in straight uniform compound channel flow. *J Hydraul Eng* 131(3):175–183

7. Prinos P, Townsend RD (1984) Comparison of methods for predicting discharge in compound open channels. *Adv Water Resour* 7(4):180–187
8. Wormleaton PR, Merrett DJ (1990) An improved method of calculation for steady uniform flow in prismatic main channel/flood plain sections. *J Hydraul Res* 28(2):157–174
9. Christodoulou GC (1992) Apparent shear stress in smooth compound channels. *Water Resour Manag* 6(3):235–247
10. Huthoff F, Roos PC, Augustijn DC, Hulscher SJ (2008) Interacting divided channel method for compound channel flow. *J Hydraul Eng* 134(8):1158–1165
11. Moreta PJ, Martin-Vide JP (2010) Apparent friction coefficient in straight compound channels. *J Hydraul Res* 48(2):169–177
12. Chen Z, Chen Q, Jiang L (2016) Determination of apparent shear stress and its application in compound channels. *Procedia Eng* 154:459–466
13. Tang X (2019) A new apparent shear stress-based approach for predicting discharge in uniformly roughened compound channels. *Flow Meas Instrum* 65:280–287
14. Knight DW, Demetriou JD (1983) Flood plain and main channel flow interaction. *J Hydraul Eng* 109(8):1073–1092
15. Knight DW, Hamed ME (1984) Boundary shear in symmetrical compound channels. *J Hydraul Eng* 110(10):1412–1430
16. Tominaga A, Nezu I (1991) Turbulent structure in compound open-channel flows. *J Hydraul Eng* 117(1):21–41
17. Fernandes JN (2013) Compound channel uniform and non-uniform flows with and without vegetation in the floodplain, Doctoral dissertation, Departamento de Engenharia Civil 599 Instituto Superior Técnico da Universidade Técnica de Lisboa, Portugal
18. Blanckaert K, Duarte A, Schleiss AJ (2010) influence of shallowness, bank inclination and bank roughness on the variability of flow patterns and boundary shear stress due to secondary currents in straight open-channels. *Adv Water Resour* 33(9):1062–1074
19. Kara S, Stoesser T, Sturm TW (2012) Turbulence statistics in compound channels with deep and shallow overbank flows. *J Hydraul Res* 50(5):482–493
20. Atabay S (2001) Stage-discharge, resistance and sediment transport relationships for flow in straight compound channels, Doctoral dissertation, University of Birmingham, United Kingdom
21. Proust S, Fernandes JN, Peltier Y, Leal JB, Rivière N, Cardoso AH (2013) Turbulent non-uniform flows in straight compound open-channels. *J Hydraul Res* 51(6):656–667
22. Yule AJ (1971) Two-dimensional self-preserving turbulent mixing layers at different free stream velocity ratios, Report. HM Stationery Office, Department of the Mechanics of Fluids, University of Manchester, United Kingdom
23. Brown GL, Roshko A (1974) On density effects and large structure in turbulent mixing layers. *J Fluid Mech* 64(4):775–816
24. Uijtewaal WSJ, Booij R (2000) Effects of shallowness on the development of free-surface mixing layers. *Phys Fluids* 12(2):392–402
25. Bousmar D (2002) Flow modelling in compound channels. *Unire de Genie Civil et Environnemental*
26. Rajaratnam N, Ahmadi R (1981) Hydraulics of channel with floodplains. *J Hydraul Res* 19(1):43–60
27. Myers WRC (1978) Momentum transfer in a compound channel. *J Hydraul Res* 16(2):139–150
28. James M, Brown BJ (1977) Geometric parameters that influence floodplain flow, Report No. WES-RR-H-77-1. Army Engineer Waterways Experiment Station, Vicksburg Miss
29. Knight DW, Demetriou JD, Hamed ME (1983) Hydraulic analysis of channels with floodplains, In: Proceedings of international conference on the hydraulic aspects of floods and flood control, BHRA fluid engineering, Bedford 1983: 129–144, [https://doi.org/10.1061/\(ASCE\)0733-9429\(1983\)109:8\(1073\)](https://doi.org/10.1061/(ASCE)0733-9429(1983)109:8(1073))
30. Joo CBH, Seng DMY (2008) Study of flow in a non-symmetrical compound channel with rough flood plain. *J Inst Eng* 69(2):18–26
31. Al-Khatib IA, Abaza KA, Khatib JI (2015) An empirical discharge prediction model for smooth asymmetric compound rectangular channel validated using area method. *ISH J Hydraul Eng* 21(3):231–241
32. Farooq R, Ahmad W, Hashmi HN, Saeed Z (2016) Computation of momentum transfer coefficient and conveyance capacity in asymmetric compound channel. *Arab J Sci Eng* 41(10):4225–4234. <https://doi.org/10.1007/s13369-016-2173-8>
33. Thornton C, Abt S, Morris C, Fischenich J (2000) Calculating shear stress at channel-overbank interfaces in straight channels with vegetated floodplains. *J Hydraul Eng* 126:929–936
34. Hamidifar H, Keshavarzi A, Omid MH (2016) Evaluation of 1-D and 2-D models for discharge prediction in straight compound channels with smooth and rough floodplain. *Flow Meas Instrum* 49:63–69

35. Valyrakis M, Liu D, Turker U, Yagci O (2021) The role of increasing riverbank vegetation density on flow dynamics across an asymmetrical channel. *Environ Fluid Mech* 21(3):643–666
36. Wang J, Liu X, Min F, Dai J, Jiang X (2022) Turbulence structure and longitudinal velocity distribution of open channel flows with reedy emergent vegetation. *Ecohydrology* 15(1):e2352
37. Rahim AS, Yonesi HA, Shahinejad B, Podeh HT, Azamattulla HM (2022) Flow structures in asymmetric compound channels with emergent vegetation on divergent floodplain. *Acta Geophys* 70:1–19
38. Uehlinger UF, Wantzen KM, Leuven RS, Arndt H (2009) The Rhine river basin, 686 245, ISBN 9780123694492, <https://doi.org/10.1016/B978-0-12-369449-2.00006-0>
39. Tockner K, Uehlinger U, Robinson CT (2009) *Rivers of Europe*. Academic Press, Cambridge
40. Ellis N, Brazier R, Anderson K (2021) Comparing fine-scale structural and hydrologic connectivity within unimproved and improved grassland. *Ecohydrology* 14(7):e2330
41. Nezu I, Onitsuka K, Iketani K (1999) Coherent horizontal vortices in compound open-channel flows. *Hydraulic modeling*, pp 17–32
42. Stocchino A, Brocchini M (2010) Horizontal mixing of quasi-uniform straight compound channel flows. *J Fluid Mech* 643:425
43. Shiono K, Knight DW (1991) Turbulent open-channel flows with variable depth across the channel. *J Fluid Mech* 222:617–646
44. Bousmar D, Zech Y (1999) Momentum transfer for practical flow computation in compound channels. *J Hydraul Eng*. [https://doi.org/10.1061/\(ASCE\)0733-9429\(1999\)125:7\(696\),696-706](https://doi.org/10.1061/(ASCE)0733-9429(1999)125:7(696),696-706)
45. Proust S, Bousmar D, Riviere N, Paquier A, Zech Y (2009) Nonuniform flow in compound channel: a 1-D method for assessing water level and discharge distribution. *Water resources research*, 45(12)
46. Proust S, Bousmar D, Riviere N, Paquier A, Zech Y (2010) Energy losses in compound open channels. *Adv Water Resour* 33(1):1–16
47. Abril JB, Knight DW (2004) Stage-discharge prediction for rivers in flood applying a depth-averaged model. *J Hydraul Res* 42(6):616–629
48. Knight D (2013) *Hydraulic problems in flooding: from data to theory and from theory to practice, experimental and computational solutions of hydraulic problems: 32nd international school of hydraulics*, Springer Berlin Heidelberg, Germany
49. Wang W, Huai Wx, Gao M (2014) Numerical investigation of flow through vegetated multi-stage compound channel. *J Hydrodyn* 26:467–473. [https://doi.org/10.1016/S1001-6058\(14\)60053-6](https://doi.org/10.1016/S1001-6058(14)60053-6)
50. Abernethy B, Rutherford ID (2001) The distribution and strength of riparian tree roots in relation to riverbank reinforcement. *Hydrol Process* 15(1):63–79
51. Wu W, He Z (2009) Effects of vegetation on flow conveyance and sediment transport capacity. *Int J Sedim Res* 24(3):247–259
52. Devi K, Khatua KK, Das BS (2016) Apparent shear in an asymmetric compound channel. *River Flow 2016: Iowa City, USA, July 11–14, 2016*, 48. <https://www.taylorfrancis.com/books/9781317289128>
53. Fernandes JN, Leal JB, Cardoso AH (2011) Apparent friction coefficient in straight compound channels. *J Hydraul Res* 49(6):836–838. <https://doi.org/10.1080/00221686.2011.618058>
54. Bousmar D, Proust S, Zech Y (2006) September, Experiments on the flow in an enlarging compound channel. In: *River Flow 2006: Proceedings of the international conference on fluvial hydraulics*, Lisbon, Portugal, 6–8 September 2006 (pp 323–332). Leiden, Netherlands: Taylor and Francis
55. Goring DG, Nikora VI (2002) Despiking acoustic Doppler velocimeter data. *J Hydraul Eng* 128(1):117–126
56. Soldini L, Piattella A, Mancinelli A, Bernetti R, Brocchini M (2004) Macro-vortices-induced horizontal mixing in compound channels. *Ocean Dyn* 54(3–4):333–339
57. Chu VH, Babarutsi S (1988) Confinement and bed-friction effects in shallow turbulent mixing layers. *J Hydraul Eng* 114(10):1257–1274
58. Wood DH, Bradshaw P (1984) A turbulent mixing layer constrained by a solid surface. Part 2. Measurements in the wall-bounded flow. *J Fluid Mech* 139:347–361
59. White BL, Nepf HM (2007) Shear instability and coherent structures in shallow flow adjacent to a porous layer. *J Fluid Mech* 593:1–32
60. Proust S, Nikora VI (2020) Compound open-channel flows: effects of transverse currents on the flow structure. *J Fluid Mech* 885:A24
61. Wang F, Huai W, Guo Y, Liu M (2021) Turbulence structure and momentum exchange in compound channel flows with shore ice covered on the floodplains. *Water Resour Res* 57(4):e2020WR028621
62. Kim J, Moin P, Moser R (1987) Turbulence statistics in fully developed channel flow at low Reynolds number. *J Fluid Mech* 177:133–166
63. Wallace JM, Eckelmann H, Brodkey RS (1972) The wall region in turbulent shear flow. *J Fluid Mech* 54(1):39–48
64. Willmarth WW, Lu SS (1972) Structure of the Reynolds stress near the wall. *J Fluid Mech* 55(1):65–92

65. White BL, Nepf HM (2008) A vortex-based model of velocity and shear stress in a partially vegetated shallow channel. *Water Resour Res*. <https://doi.org/10.1029/2006WR005651>
66. Tamai N, Asaeda T, Ikeda H (1986) Study on generation of periodical large surface eddies in a composite channel flow. *Water Resour Res* 22(7):1129–1138
67. Knight DW, Omran M, Tang X (2007) Modeling depth-averaged velocity and boundary shear in trapezoidal channels with secondary flows. *J Hydraul Eng* 133(1):39–47
68. Xiaohui S, Li CW (2002) Large eddy simulation of free surface turbulent flow in partly vegetated open channels. *Int J Numer Meth Fluids* 39(10):919–937
69. Macintosh JC (1990) Hydraulic characteristics in channels of complex cross-section. Ph.D. dissertation, University of Queensland
70. Al-Khatib IA, Gogus M (2014) Prediction models for discharge estimation in rectangular compound broad-crested weirs. *Flow Meas Instrum* 36:1–8
71. Truong SH, Uijttewaal WSJ (2019) Transverse momentum exchange induced by large coherent structures in a vegetated compound channel. *Water Resour Res* 55(1):589–612

Publisher's Note Springer Nature remains neutral with regard to jurisdictional claims in published maps and institutional affiliations.

Springer Nature or its licensor (e.g. a society or other partner) holds exclusive rights to this article under a publishing agreement with the author(s) or other rightsholder(s); author self-archiving of the accepted manuscript version of this article is solely governed by the terms of such publishing agreement and applicable law.